



## A CFD-DEM study of hydrodynamics with heat transfer in a gas-solid fluidized bed reactor for solar thermal applications

Selvan Bellan <sup>a,c,\*</sup>, Koji Matsubara <sup>b,c</sup>, Hyun Seok Cho <sup>a,c</sup>, Nobuyuki Gokon <sup>a,c</sup>, Tatsuya Kodama <sup>b,c</sup>

<sup>a</sup> Center for Transdisciplinary Research, Niigata University, 8050 Ikarashi 2-nocho, Niigata 950-2181, Japan

<sup>b</sup> Faculty of Engineering, Niigata University, 8050 Ikarashi 2-nocho, Niigata 950-2181, Japan

<sup>c</sup> Pacific Rim Solar Fuels Research Center, Niigata University, 8050 Ikarashi 2-nocho, Niigata 950-2181, Japan



### ARTICLE INFO

#### Article history:

Received 6 June 2017

Received in revised form 3 September 2017

Accepted 6 September 2017

Available online 17 October 2017

#### Keywords:

Solar receiver

CFD-DEM modeling

Fluidized bed

Particle-fluid flow

Beam-down solar concentrating system

### ABSTRACT

The particles flow and heat transfer characteristics of a high temperature solar thermochemical fluidized bed reactor have been studied for solar beam-down concentrating systems. A numerical model has been developed by the combined approach of computational fluid dynamics (CFD) and discrete element method (DEM) collisional model since it is an effective approach for studying the gas-solid flow. The discrete ordinate model has been used to solve the radiation heat transfer. An experimental visualization of particles circulation pattern and mixing of two-tower fluidized bed system has been presented. A good agreement has been found between the experimental measurements and numerical predictions. The effect of gas superficial velocity, bed mass and inlet gas temperature on the flow pattern and temperature characteristics of the bed have been investigated. The results showed that the maximum and average temperature of the bed, depends on the top layer position and focal point of the concentrated radiation, decreased when increasing the total mass of the bed.

© 2017 Elsevier Ltd. All rights reserved.

## 1. Introduction

In solar thermochemical applications of dense gas-solid fluidized beds, mixing and segregation processes play a vital role on reaction rate and efficiency. The mixing and segregation behavior of fluidized beds is determined by the particles flow characteristics and bubble dynamics [1–4]. Considerable efforts have been made to develop advanced techniques for measuring dynamics of dense gas-solid flow in fluidized beds such as particle image velocimetry (PIV), digital image analysis (DIA), positron emission particle tracking, magnetic resonance imaging, electrical capacitance tomography, etc. However, it's pretty challenging to obtain accurate flow characteristics at reasonable cost [5]. With rapid advancements of computers and numerical algorithms, CFD has become a powerful tool to obtain the flow characteristics of the dense gas-solid flow quantitatively. Various numerical models have been developed in the past few decades to simulate the gas-solid flows. The most widely used models are Eulerian-Eulerian and Eulerian-Lagrangian models.

In discrete particle model, the particle collisions can be either modelled by soft sphere or hard sphere approach. Initially, Tsuji

et al. [6] developed a two dimensional CFD-DEM model for fluidized bed by soft sphere approach. Following their study, various researchers have improved that model extensively with some modifications in the past two decades. In the early stages, the number of simulation particles was several thousand only but now with the vast improved computers and techniques, up to 100,000 particles can be simulated with single core processor. By parallel computing, fluidized bed systems consisting of several million particles have been simulated for different kinds of problems [7,8]. Multi-physics problems coupled with heat transfer and chemical reactions were investigated [9–11]. Turbulent models were coupled with fluidized bed models [12,13]. The dependency of particle-particle collision on turbulence characteristics, such as turbulent kinetic energy (TKE), dissipation rate (TDR), fluctuation and correlated fluctuations were studied [12]. In order to reduce the computational cost, various effective methods and algorithms were proposed [14–16]. Particle-gas flow of complex geometries were investigated [17,18].

Fluidized bed reactors have been used as receiver and storage systems of concentrated solar plants, which is one of the promising technologies currently undergoing rapid development [19,20]. Solar particle receivers (SPR) were developed to drive the concentrating solar plants (CSP) at higher operating temperatures and enhance the efficiency of the power cycles. The SPR-based CSP system uses solid particles as the heat transfer medium (HTM) in

\* Corresponding author at: Center for Transdisciplinary Research, Niigata University, 8050 Ikarashi 2-nocho, Niigata 950-2181, Japan.

E-mail address: [selvan@eng.niigata-u.ac.jp](mailto:selvan@eng.niigata-u.ac.jp) (S. Bellan).

place of currently used molten salt or steam [21,22]. An experimental and theoretical study of a pilot scale solar fluidized bed receiver was carried out by Flamant et al. [21] at the early stage of development using alumina particles, and the unsteady behavior of the receiver in the temperature range of 550–915 °C was described by a simple heat transfer model. In order to improve thermal performance of fluidized beds for concentrated solar power plants and thermal energy storage applications, various numerical and experimental investigations were carried out [23–26]. In concentrated solar thermal industry, fluidized-bed technology has also been used to produce hydrogen by thermochemical two step water splitting cycles [19], and synthetic gas by gasification of coal coke [27]. Recently, couple of fluidized bed reactors have been developed for two-step thermochemical water splitting cycles and coal coke gasification [28–30] using 100 kW beam-down demonstration plant at Miyazaki, Japan. A tubular fluidized receiver for beam-down solar concentrating system was developed by Matsubara et al. [31]. The fluid dynamics of the prototype receiver was experimentally investigated by 3 kW solar simulator. Subsequently, A two-tower fluidized bed system filled with spherical non-reacting particles has been proposed [32] to use concurrently as receiver and storage system as shown in Fig. 1a.

Despite many studies on the CFD-DEM modeling of fluidized beds for various applications, only a few studies have been reported on modeling and validation of fluidized beds for concentrated solar reactor/receiver. To the best of our knowledge, the CFD-DEM model of two-tower fluidized bed receiver for beam down solar concentrating system has not been developed and studied considerably. Furthermore, the thermo-chemical reaction/storage of the two-tower reactor strongly depends on the concentrated radiation obtained through the top slit of the left tower. The intensity of the radiation is according to the sunlight which depends on the time of the day. Thus, an appropriate flow pattern and the velocity of the circulation should be given according to the sunlight availability (irradiation power). Hence, the complete flow characteristics of the two-tower receiver is required to implement the proposed concept. Accordingly, in this study, the Euler-Lagrange model has been developed to investigate the influence

of gas velocity, gas temperature, incident radiation and bed mass on the flow characteristics, particles flow pattern and temperature of the two-tower reactor.

## 2. Modeling of gas-solid flow

To simulate the hydrodynamics of the gas-solid flow, the Euler-Lagrange model is developed, which treats the fluid phase as a continuous fluid and the particle phase as discrete elements. The flow of the gas-phase is solved based on the Navier-Stokes equations, while the particle movement is solved using Newton's equation of motion.

### 2.1. Gas phase modeling

The mass conservation for gas phase is included by multiplying each term of the standard continuity equation with the corresponding volume fraction of gas phase as given below:

$$\frac{\partial}{\partial t}(\alpha_f \rho_f) + \nabla \cdot (\alpha_f \rho_f \vec{u}_f) = 0 \quad (1)$$

where  $\alpha_f$ ,  $\rho_f$  and  $\vec{u}_f$  are volume fraction, density and velocity of gas phase respectively. The momentum conservation equation is extended by the volume fraction and the interaction term  $F_{DEM}$ , which couples the gas phase with the corresponding solid phase. The gas phase momentum equation can be written as:

$$\frac{\partial}{\partial t}(\alpha_f \rho_f \vec{u}_f) + \nabla \cdot (\alpha_f \rho_f \vec{u}_f \vec{u}_f) = -\alpha_f \nabla p + \nabla \cdot (\alpha_f \bar{\tau}_f) + \alpha_f \rho_f \vec{g} + \vec{F}_{DEM} \quad (2)$$

where  $p$  and  $\vec{g}$  are the pressure and acceleration due to gravity respectively. The stress-strain tensor of gas phase is given as;

$$\bar{\tau}_f = \alpha_f \mu_f (\nabla \vec{u}_f + \nabla \vec{u}_f^T) + \alpha_f \left( \lambda_f - \frac{2}{3} \mu_f \right) \nabla \cdot \vec{u}_f \bar{\vec{I}} \quad (3)$$

where  $\mu_f$  and  $\lambda_f$  are respectively shear and bulk viscosity of the gas phase and  $\bar{\vec{I}}$  is the unit vector. The coupling term  $F_{DEM}$  considers the

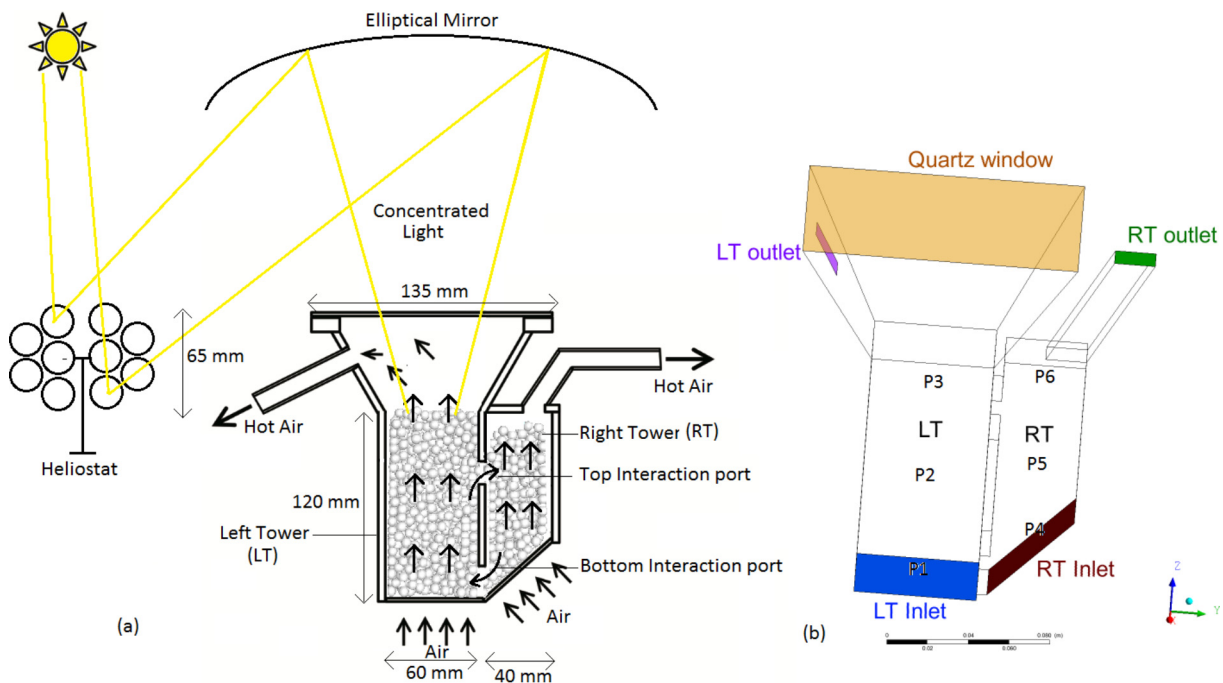


Fig. 1. (a) Schematic of the beam-down concentrated receiver/reactor and (b) computational domain.

momentum change of all particles located within one cell and is given as:

$$F_{DEM} = \sum \beta(\vec{u}_p - \vec{u}_f) \quad (4)$$

the inter-phase momentum transfer coefficient,  $\beta$ , is computed by the Ergun [33], and Wen and Yu [34] correlations for dense regimes and diluted regimes respectively as given below;

$$\beta = 150 \frac{(1 - \alpha_f)^2 \mu_f}{\alpha_f d_p^2} + 1.75(1 - \alpha_f) \frac{\rho_f}{d_p} |\vec{u}_f - \vec{u}_p| \quad \text{if } \alpha_f < 0.8 \quad (5)$$

$$\beta = \frac{3}{4} C_D \frac{\alpha_f (1 - \alpha_f)}{d_p} \rho_f |\vec{u}_f - \vec{u}_p| \alpha_f^{-2.65} \quad \text{if } \alpha_f > 0.8 \quad (6)$$

where  $C_D$  and  $d_p$  are drag coefficient and diameter of the particle respectively. The energy conservation equation for gas phase is given by

$$\begin{aligned} \frac{\partial}{\partial t} (\alpha_f \rho_f C_p T_f) + \nabla \cdot (\alpha_f \rho_f \vec{u}_f C_p f T_f) \\ = \nabla \cdot (\alpha_f k_{f,eff} \nabla T_f) + Q_p + Q_{others} \end{aligned} \quad (7)$$

where  $C_p$ ,  $T_f$  and  $k_{f,eff}$  are specific heat, temperature and effective thermal conductivity of the gas phase respectively.  $Q_p$  is the heat exchange between the gas phase and solid phase, and  $Q_{others}$  is a source term that includes sources of enthalpy due to radiation.

## 2.2. Discrete particle phase

In this model, the moving particles are considered as moving mass points and the fluid flow details around the particles, such as boundary layers, vortex shedding, are neglected. The motion of a spherical particle with mass  $m_p$  and moment of inertia  $I_p$  is described by Newton's equations;

$$m_p \frac{d\vec{u}_p}{dt} = \vec{F}_{aero} + \vec{F}_g + \vec{F}_{con}^n + \vec{F}_{con}^t \quad (8)$$

$$I_p \frac{d\vec{\omega}_p}{dt} = \tau_p \quad (9)$$

where  $\omega_p$  is the particle angular velocity,  $\tau_p$  is the torque applied to the particle in fluid domain,  $m_p$  is particle mass and  $u_p$  is the particle velocity. The volume force ( $\vec{F}_g$ ) includes the forces acting on the suspended particle due to gravity and buoyancy. The aerodynamic forces ( $\vec{F}_{aero}$ ) comprise the drag, pressure gradient, virtual mass, Saffman and Magnus forces. Usually, the main force exerted by the fluid on the particle is the drag force. The virtual mass force, which accounts for inertial effects of the surrounding fluid. Saffman and Magnus forces of rotating particles are not considered in this model since the density of gas is low. The contact forces  $\vec{F}_{con}^n$  and  $\vec{F}_{con}^t$  respectively describe the normal and tangential forces that occur during particle-particle or particle-wall collisions, and are computed based on the linear-spring and dashpot model. The principle methodology is known as the soft-sphere approach in which two particles can overlap each other. Based on the spring constant and the overlap magnitude, the normal contact force due to elastic deformations can be calculated. The dashpot terms allow for the modelling of inelastic or elastic collisions using the coefficient of restitution. The normal force is thus calculated according to Ansys Inc. [35]:

$$\vec{F}_{con,i}^n = (K\delta + \gamma(\vec{v}_{ij} \cdot \vec{n}_{ij}))\vec{n}_{ij} \quad (10)$$

where

$$\gamma = \frac{-2m_{ij} \ln(\eta)}{t_{coll}} \quad (11)$$

$$m_{ij} = \frac{m_i m_j}{m_i + m_j} \quad (12)$$

$$\vec{v}_{ij} = \vec{v}_j - \vec{v}_i \quad (13)$$

$$t_{coll} = f_{loss} \sqrt{\frac{m_{ij}}{k}} \quad (14)$$

$$f_{loss} = \sqrt{\pi^2 + \ln^2 \eta} \quad (15)$$

In the above equations  $K$ ,  $\gamma$ ,  $m_{ij}$ ,  $t_{coll}$ ,  $f_{loss}$ ,  $\delta$ ,  $n_{ij}$  and  $v_{ij}$  are respectively spring constant, the damping coefficient, reduced mass, collision time scale, loss factor, overlap, unit vector and the relative velocity between particle  $i$  and particle  $j$ . The force on particle  $j$  is calculated by

$$\vec{F}_{con,j}^n = -\vec{F}_{con,i}^n \quad (16)$$

Using the Coulomb friction collision law, the tangential collision forces are calculated:

$$\vec{F}_{con,i}^t = \mu \vec{F}_{con,i}^n \quad (17)$$

The direction of tangential force,  $\vec{F}_{con,i}^t$ , is opposite to the relative tangential motion. The friction coefficient  $\mu$  is a function of the relative tangential velocity magnitude  $|v_r|$  and is calculated as follows:

$$\mu(v_r) = \begin{cases} \mu_{stick} + (\mu_{stick} - \mu_{glide}) \\ \left( \frac{|v_r|}{v_{glide}} - 2 \right) \left( \frac{|v_r|}{v_{glide}} \right) & \text{if } |v_r| \leq v_{glide} \\ \mu_{glide} & \text{if } v_{glide} < |v_r| \leq v_{limit} \\ \frac{(1+v_{ratio})}{1+\mu_{ratio}v_{ratio}} & \text{if } |v_r| > v_{limit} \end{cases} \quad (18)$$

where

$$v_{ratio} = \frac{(|v_r| - v_{limit})}{s_{limit}} \quad (19)$$

$$\mu_{ratio} = \frac{\mu_{glide}}{\mu_{limit}} \quad (20)$$

where  $\mu_{stick}$ ,  $\mu_{glide}$  and  $\mu_{limit}$  are the sticking friction coefficient, gliding friction coefficient and high velocity limit friction coefficient respectively.  $v_{glide}$  is the gliding velocity and  $v_{limit}$  is the limit velocity. The variable  $s_{limit}$  is determined based on how fast ( $v_r$ ) approaches  $\mu_{limit}$ .

The energy balance equation to relate the particle temperature,  $T_p$ , with the convective heat transfer and the absorption/emission of radiation at the particle surface is given by:

$$m_p C_{p,s} \frac{dT_p}{dt} = h A_p (T_f - T_p) + \epsilon_p A_p \sigma (\theta_R^4 - T_p^4) \quad (21)$$

where  $C_{p,s}$ ,  $T_p$ ,  $A_p$  and  $\epsilon_p$  are respectively specific heat capacity, temperature, surface area and emissivity of the particle. The heat transfer coefficient,  $h$ , is calculated by the empirical correlation given by Gunn [36]:

$$\begin{aligned} Nu = (7 - 10\alpha_f + 5\alpha_f^2)[1 + 0.7Re_p^{0.2}Pr^{0.33}] + (1.33 - 2.40\alpha_f \\ + 1.20\epsilon_f^2)Re_p^{0.7}Pr^{0.33} \end{aligned} \quad (22)$$

where  $Pr$  is Prandtl number of the continuous phase and  $Re_p$  is the Reynolds number based on the particle diameter and relative velocity. The radiation temperature is evaluated by

$$\theta_R = \left( \frac{G}{4\sigma} \right)^{1/4} \quad (23)$$

where  $G$  and  $\sigma$  are the incident radiation and Stefan-Boltzmann constant respectively.

### 2.3. Radiation model

The radiative transfer equation for an absorbing, emitting and scattering medium at position  $\vec{r}$  in the direction  $\vec{s}$  can be expressed as

$$\frac{dI(\vec{r}, \vec{s})}{ds} = (a + \sigma_s)I(\vec{r}, \vec{s}) - an^2 \frac{\sigma T_f^4}{\pi} + \frac{\sigma_s}{4\pi} \int_0^{4\pi} I(\vec{r}, \vec{s}')\varphi(\vec{s}, \vec{s}')d\Omega' \quad (24)$$

where  $I$ ,  $a$ ,  $\sigma_s$ ,  $n$ ,  $\varphi$ ,  $\vec{s}'$  and  $\Omega'$  are radiative intensity, absorption coefficient, scattering coefficient, refractive index, phase function, direction vector and solid angle respectively. In this study, discrete ordinates (DO) radiation model has been used to solve the radiative transfer equation for a finite number of discrete solid angles, each associated with vector direction  $\vec{s}$  fixed in the global Cartesian system ( $x$ ,  $y$ ,  $z$ ). The discrete ordinate model considers the radiative transfer equation (RTE) in the direction  $\vec{s}'$  as a field equation. Thus, the above equation is written as

$$\nabla \cdot (I(\vec{r}, \vec{s}) \vec{s}) + (a + \sigma_s)I(\vec{r}, \vec{s}) = an^2 \frac{T_f^4}{\pi} + \frac{\sigma_s}{4\pi} \int_0^{4\pi} I(\vec{r}, \vec{s}')\varphi(\vec{s}, \vec{s}')d\Omega' \quad (25)$$

The effect of discrete phase on radiation is included by neglecting all other sources of scattering in the fluid phase. Thus, the contribution of discrete phase appears in the radiative transfer equation as

$$\nabla \cdot (I \vec{s}) + (a + a_p + \sigma_s)I(\vec{r}, \vec{s}) = an^2 \frac{T_f^4}{\pi} + E_p + \frac{\sigma_p}{4\pi} \int_0^{4\pi} I(\vec{r}, \vec{s}')\varphi(\vec{s}, \vec{s}')d\Omega' \quad (26)$$

**Table 1**  
Boundary conditions.

Section	Boundary type	Velocity $\bar{u}_f$	Energy
LT_inlet	Velocity-inlet	Velocity (m/s)	Temperature (K)
LT wall	Wall	0.0	$q = h_{ext}(T_{ext} - T_w)$
LT outlet	Pressure outlet	$\frac{\partial \bar{u}_f}{\partial n} = 0$	$\frac{\partial T}{\partial n} = 0$
Quartz window	wall	0.0	$q = h_{ext}(T_{ext} - T_w) + \epsilon_{ext}\sigma(T_\infty^4 - T_w^4)$
RT_inlet	Velocity-inlet	Velocity (m/s)	Temperature (K)
RT wall	Wall	0.0	$q = h_{ext}(T_{ext} - T_w)$
RT outlet	Pressure outlet	$\frac{\partial \bar{u}_f}{\partial n} = 0$	$\frac{\partial T}{\partial n} = 0$

**Table 2**  
Properties of the gas and solid phase.

Properties	Gas	Particle (Geldart-B)	Particle (Geldart-D)
Density (kg/m <sup>3</sup> )	$1.245 \times 10^{-13}T^4 - 9.815 \times 10^{-10}T^3 + 2.819 \times 10^{-06}T^2 - 3.590 \times 10^{-03}T + 1.958$	1040	6870
Specific heat (J/kg-K)	$2.666 \times 10^{-07}T^3 - 1.005 \times 10^{-03}T^2 + 1.289 T + 6.206 \times 10^2$	–	456
Thermal conductivity (W/m-K)	$6.070 \times 10^{-11}T^3 - 2.295 \times 10^{-07}T^2 + 3.180 \times 10^{-04}T - 6.554 \times 10^{-2}$	–	–
Viscosity (kg/m s)	$-3.215 \times 10^{-12}T^2 + 3.952 \times 10^{-08}T + 8.548 \times 10^{-06}$	–	–
Diameter (μm)	–	700–1400	450
Shape	–	spherical	spherical
Coefficient of restitution	–	0.9	0.9
Coefficient of friction	–	0.3	0.3

where the equivalent absorption coefficient,  $a_p$ , equivalent emission,  $E_p$ , and equivalent particle scattering factor,  $\sigma_p$ , are calculated by the following equations

$$a_p = \lim_{V \rightarrow 0} \sum_{n=1}^N \epsilon_{pn} \frac{A_{pn}}{V} \quad (27)$$

$$E_p = \lim_{V \rightarrow 0} \sum_{n=1}^N \epsilon_{pn} A_{pn} \frac{\sigma T_{pn}^4}{\pi V} \quad (28)$$

$$\sigma_p = \lim_{V \rightarrow 0} \sum_{n=1}^N (1 - f_{pn})(1 - \epsilon_{pn}) \frac{A_{pn}}{V} \quad (29)$$

in the above equations, the summation is over  $N$  particles in volume  $V$ .  $T_{pn}$ ,  $\epsilon_{pn}$ ,  $f_{pn}$  are temperature, emissivity and scattering factor of particle  $n$  respectively. The projected area  $A_{pn}$  of particle  $n$  is computed by

$$A_{pn} = \frac{\pi d_{pn}^2}{4} \quad (30)$$

compared with other radiation model, DO model can fit for the entire range of optical thickness and the radiation transfer at a semi-transparent wall can be incorporated in the model.

### 2.4. Boundary and operating conditions

**Fig. 1b** shows the computational domain, formed by the region limited by the inner surface of left and right towers, top surface of perforated plates of inlets and the outlets of the left and right towers. The geometry of the fluidized bed used in numerical simulations is similar to that used in experiments for cold fluidization. The reactor walls are assumed as gray and diffuse for solving radiation heat transfer. **Table 1** shows the boundary conditions used in this model. The properties of the particles and gas are given in **Table 2**. The parameters such as spring stiffness, restitution coefficient and friction coefficient were obtained from the experimental results and literature [6].

**Table 3**  
Properties and settings of experiments and simulations used by Patil et al. [38].

Particles	
Diameter (mm)	1
Shape	Spherical
Density (kg/m <sup>3</sup> )	2500
Specific heat (J/kg K)	840
Coefficient of restitution	0.9
Coefficient of friction	0.3
Gas	
Density (kg/m <sup>3</sup> )	0.882
Specific heat (J/kg K)	1010
Viscosity (kg/m s)	$2 \times 10^{-5}$
Thermal conductivity (W/m K)	0.0346
$U_{bg}$ (m/s)	1.20 & 1.54

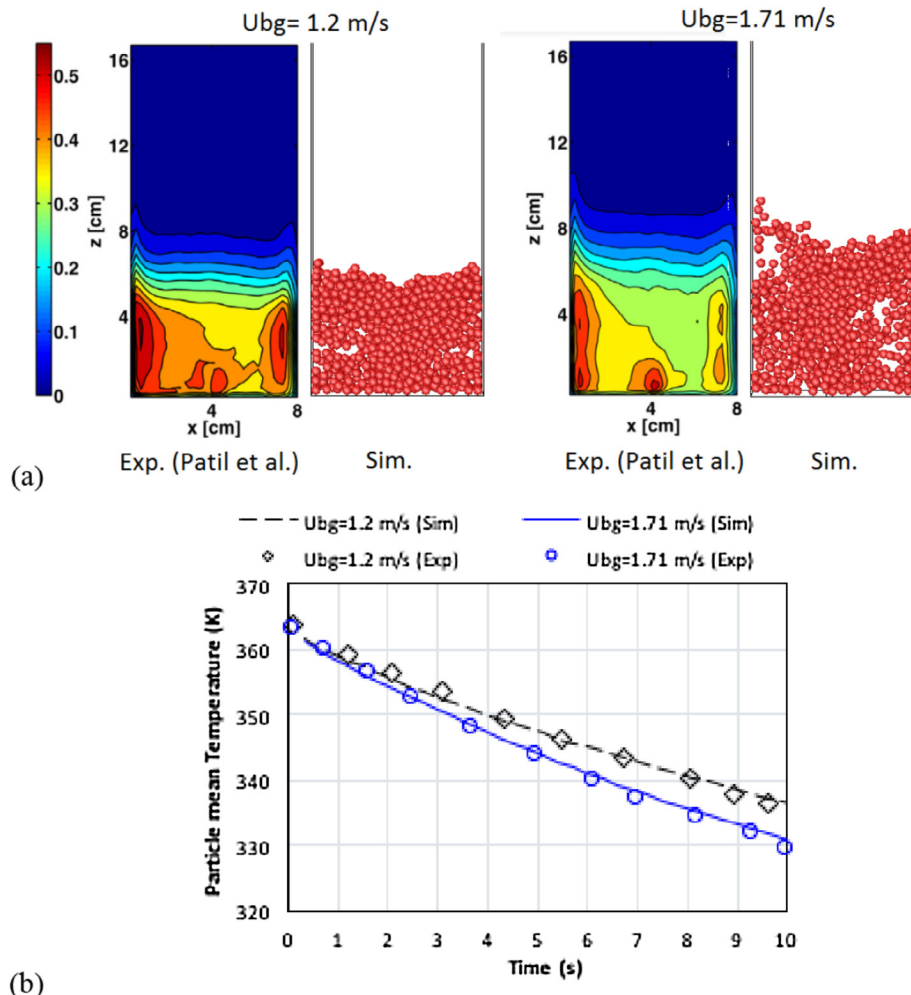


**Fig. 2.** (a) Comparison between experiments [38] and simulation for (a) solids volume fraction and (b) mean particle temperature for fluidized bed with 75 g bed mass and 1 mm particle diameter.

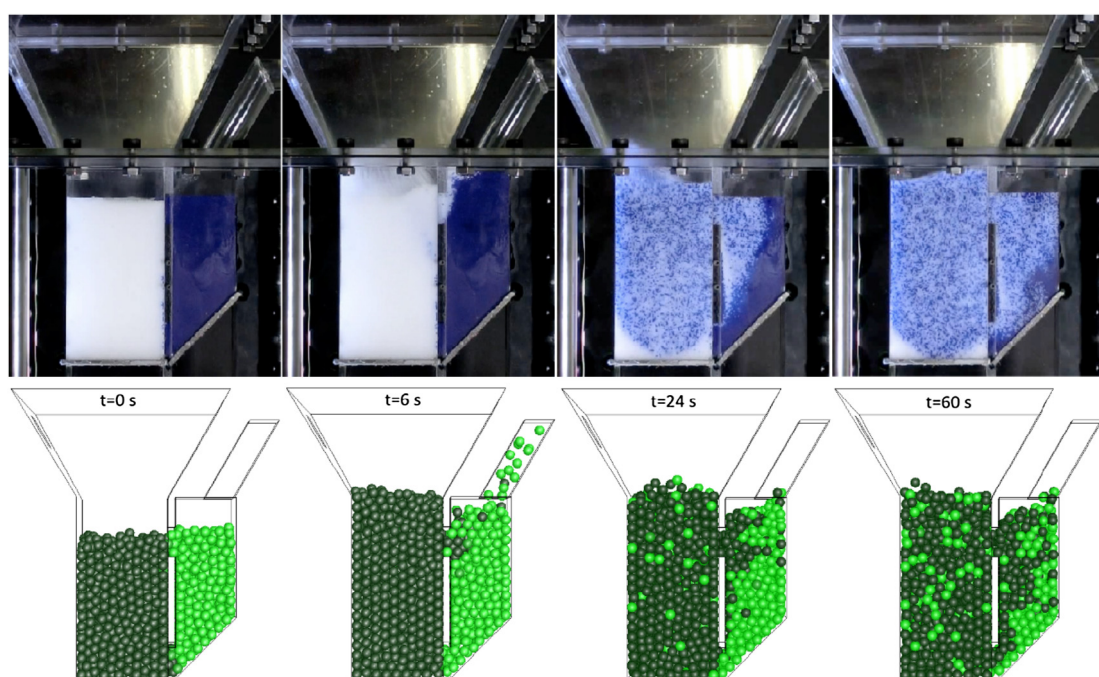


**Fig. 3.** Comparison of experimentally captured and numerically predicted flow pattern of Geldart B particles at different times.

## 2.5. Numerical approach

The governing equations were solved using a finite volume approach. Commercial code Ansys/Fluent v17 was employed for the calculations. The phase coupled SIMPLE algorithm, which is an extension of the SIMPLE algorithm to multiphase flows, was employed to treat the coupling between pressure and momentum. The QUICK scheme was used to discretize the momentum and void fraction equations. The energy equation was discretized using the first order upwind scheme. The under-relaxation factors for pressure, momentum and volume fraction were 0.9, 0.3, and 1.0, respectively. Scaled absolute residuals of  $10^{-4}$  and  $10^{-6}$  were set as the convergence criteria for continuity and momentum equations respectively. As this fluidized bed system consists of more

than one million particles, the computational cost of the collision calculation is prohibitive. Thus, in order to reduce the computational cost and track the particles in efficient manner, the parcel concept proposed by Ansys Fluent was used. Parcels are statistical representations of a number of individual particles. In this approach, the dimension of the fluid cell should be sufficiently larger than the parcel size. Based on our experience, if the fluid cell length is less than five times the diameter of the particle ( $<5d_p$ ), the solution diverges, on the contrary if the fluid cell is too large, the flow field resolution decreases. Hence, the cell length between ( $5d_p$ ) and ( $10d_p$ ) provides a good balance to tackle the aforementioned issues.

Attention was paid to the grid parameters such as maximum cell aspect ratio, cell orthogonal quality and cell skewness. Lower

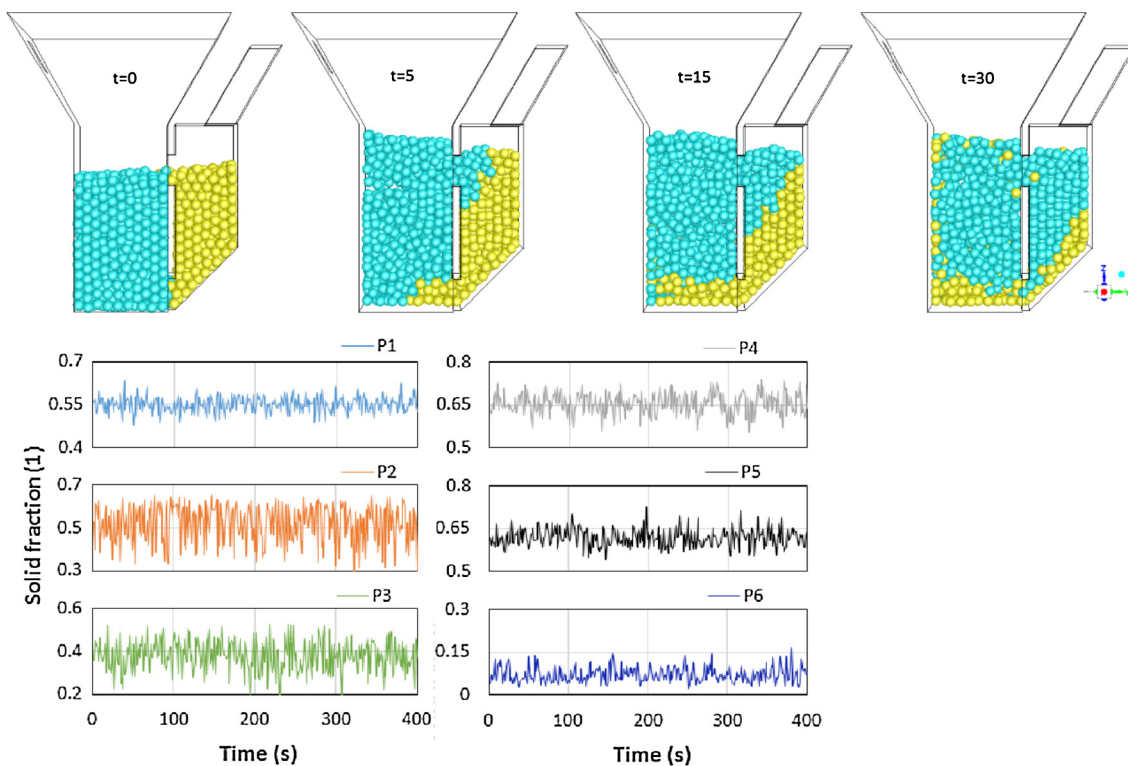


**Fig. 4.** Temporal variation of particle flow pattern and solid volume fraction at different locations.

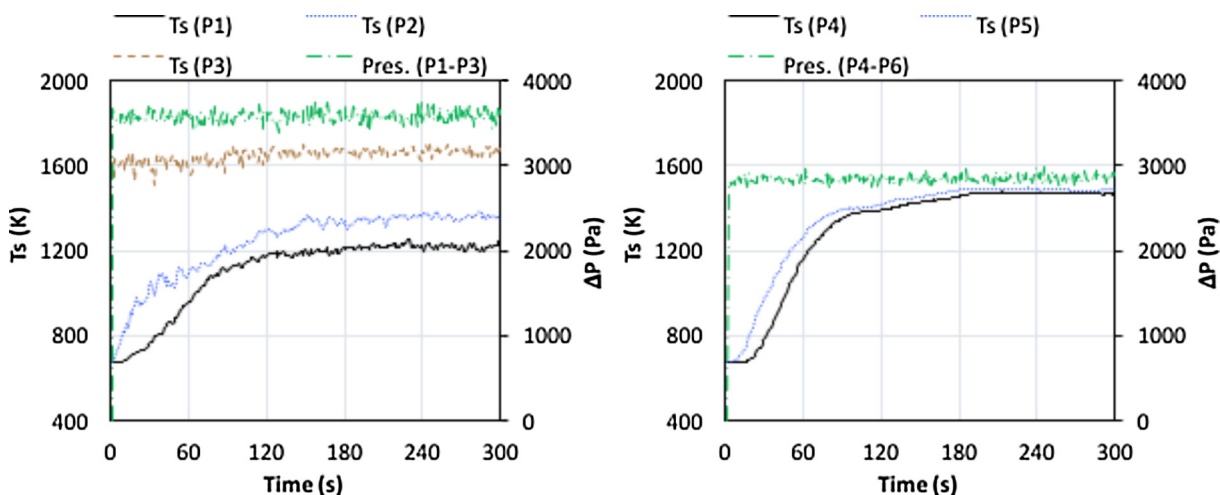


**Fig. 5.** Temperature at different locations and pressure drop of the left and right towers as a function of time.

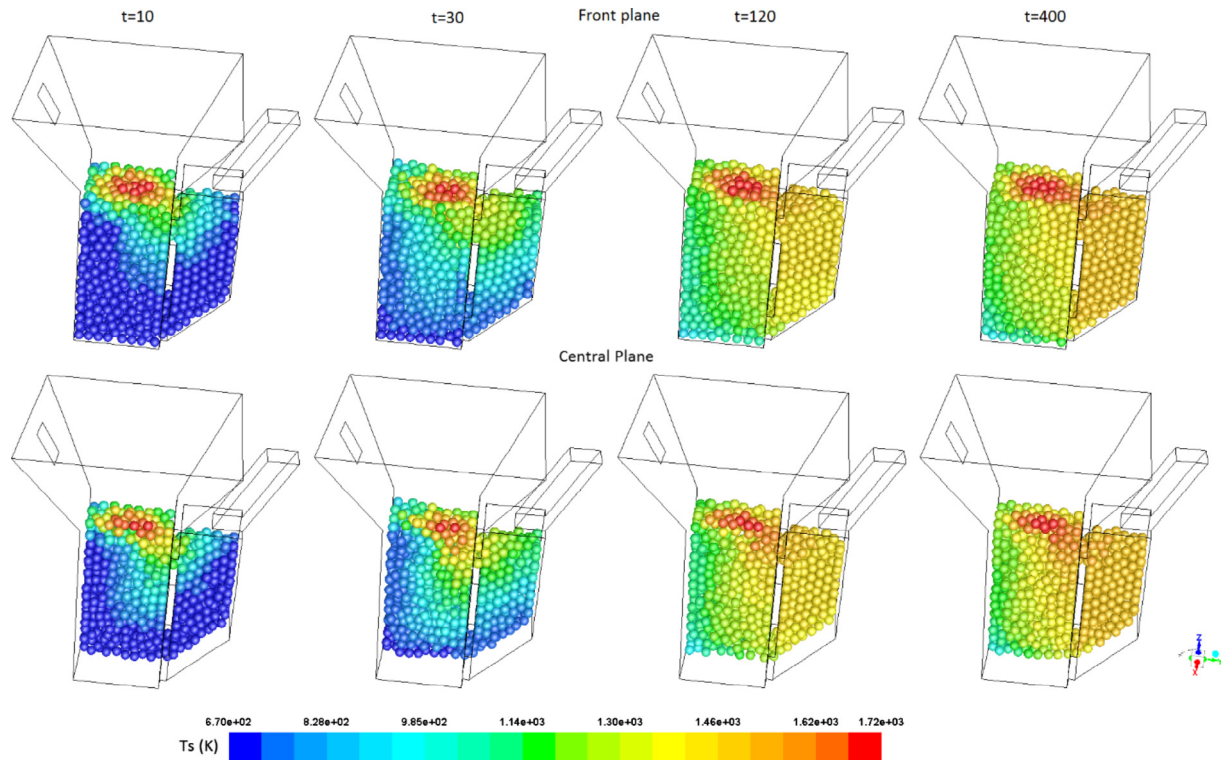


**Fig. 6.** Instantaneous temperature distribution of the bed at front and central planes.

time steps for particles are needed to properly resolve particle collisions. Higher time step sizes for particulates could result in significant overlapping of parcels and numerical instabilities. Furthermore, the particle time step should be smaller than the CFD time step. In order to obtain stable calculations, the CFD time step was maintained less than 5–10 times of the particle time step. The selection of the spring-dashpot  $K$  parameter for Particle-Particle and Particle-Wall interactions influences the particle and fluid hydrodynamics. According Cundall and Strack [37] the particle time step size should be less than the collisional time scale ( $t_{coll}$ ). In this study, the particle time step was less than five times of  $t_{coll}$  in order to catch all contact forces between parcels and walls. The node based averaging scheme was used in the particle motion solution. Linearization of source terms for the discrete phase momentum exchange were applied in order to improve numerical stability [35].

### 3. Results and discussion

#### 3.1. Comparison with experimental results for model validation

Validation has been performed by comparing the developed model results with the previously reported experimental and numerical results [38]. In their study, a series of fluidization experiments using visual/infrared imaging technique were performed on a pseudo fluidized bed setup. Hot particles were filled in a rectangular tank at room temperature, after which a constant nitrogen gas stream at 293 K was supplied through the bottom perforated plate. The setup had a small circular nozzle at the center of the perforated plate, which was closed for gas flow. Further experimental and simulation conditions and operating parameters are given in Table 3. Fig. 2 shows the comparison between the experimental data and the numerical results obtained from our simulations for the same problem. As seen in Fig. 2, reasonably good agreement is found between the numerically predicted and experimentally

obtained results, such as, solid volume fraction and particle mean temperature for two different background velocities.

Recently, couple of fluidized bed reactors have been successfully developed and tested at Niigata University, Japan, for two-step thermochemical water splitting cycles and coal coke gasification using Xe light solar simulator [28,29,39]. Following these studies, a two-tower fluidized bed system filled with spherical non-reacting particles has been proposed to use concurrently as receiver and storage system [32]. These fluidized bed systems have been developed for 100 kW<sub>th</sub> beam-down demonstration plant at Miyazaki, Japan, which consists of 88 heliostats with total area of 176 m<sup>2</sup> and an elliptical reflecting mirror at 16 m height. The schematic of the proposed beam-down reactor/receiver is shown in Fig. 1(a). Both towers filled by spherical particles. The left tower (LT) exposes to the concentrated radiation. Consequently, particles of the left tower receive radiation through the top slit and exchanges the thermal energy with particles and the heat transfer fluid. Subsequently, the heated particles gradually move to the right tower (RT) by fluidization of particles through drag force given by fluid flow with appropriate flow rate conditions at the inlets of the left and right towers.

In order to investigate the characteristics of circulating flow between the left and right towers and the influence of fluid flow rate on mixing and flow direction (clockwise or anticlockwise), a lab-scale transparent fluidized bed system has been designed (Fig. 1b) and fabricated. The left tower consists of a rectangular duct (60 mm width and depth, and 140 mm height), which is extended at the top end as frustum shape to receive radiation through the top slit. In order to prevent the asymmetric effects of the flow at the inlet of the bed, the gas is injected through a perforated stainless-steel plate. The right tower consisted of a rectangular duct (40 mm width and depth and 140 mm height) in which a perforated plate is fixed at 45° as shown in the figure.

In order to obtain the visualization of movement of particles between the two towers, two colors of polystyrene beads (Geldart

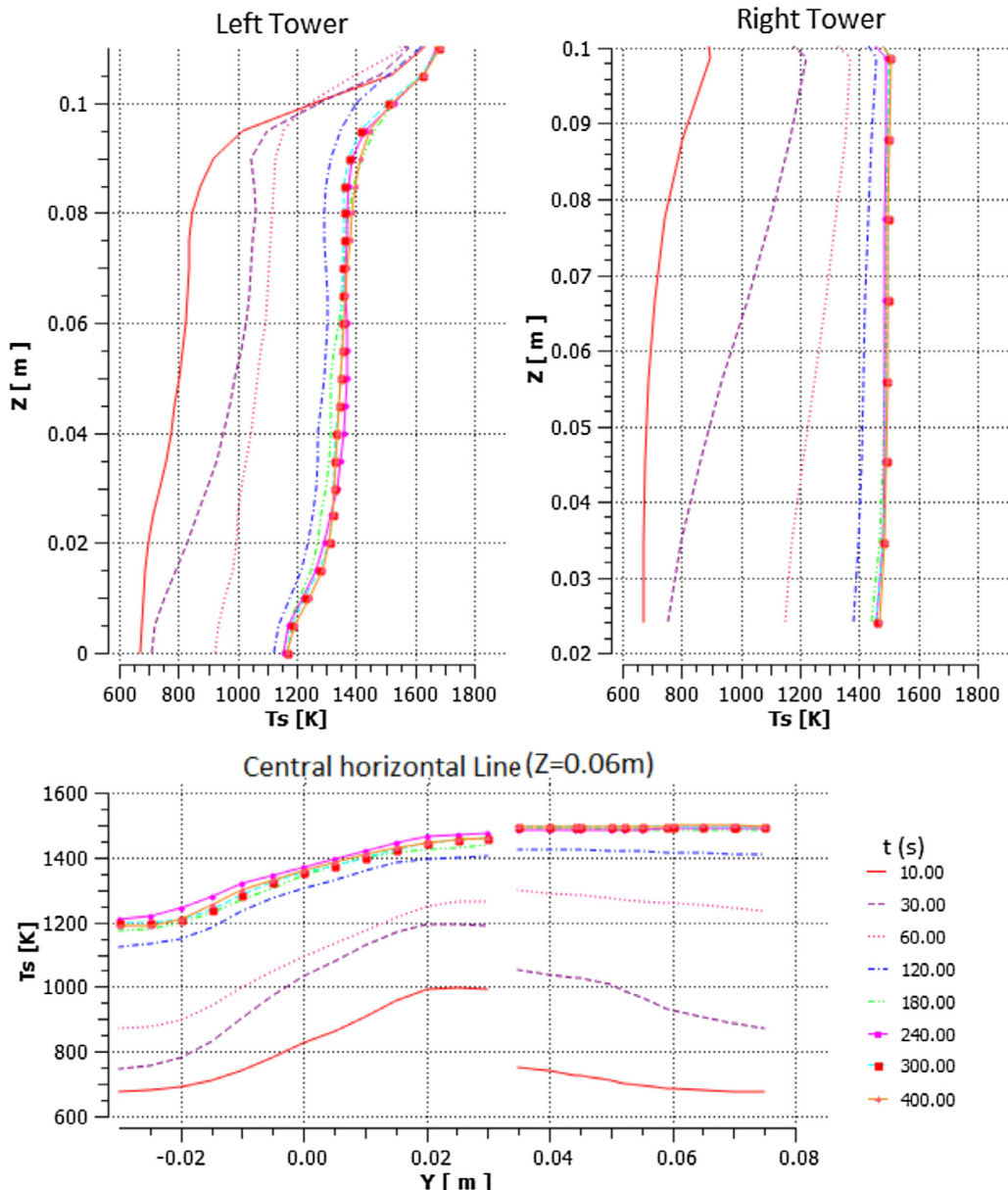


**Fig. 7.** Temperature distribution at central axial line (top) and central horizontal line (bottom) of the fluidized bed reactor at various time instances.

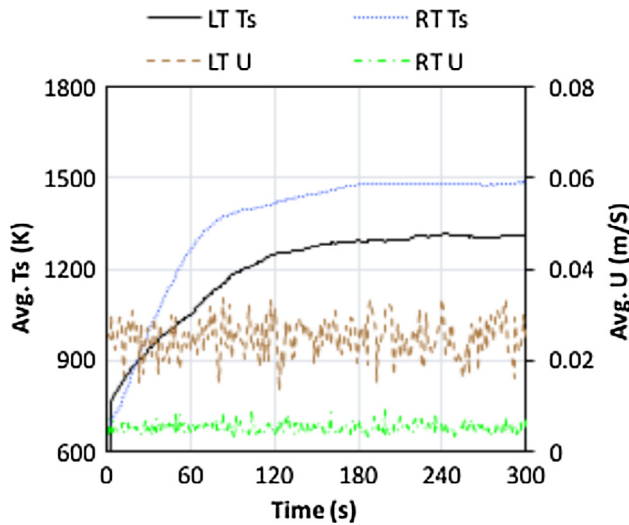


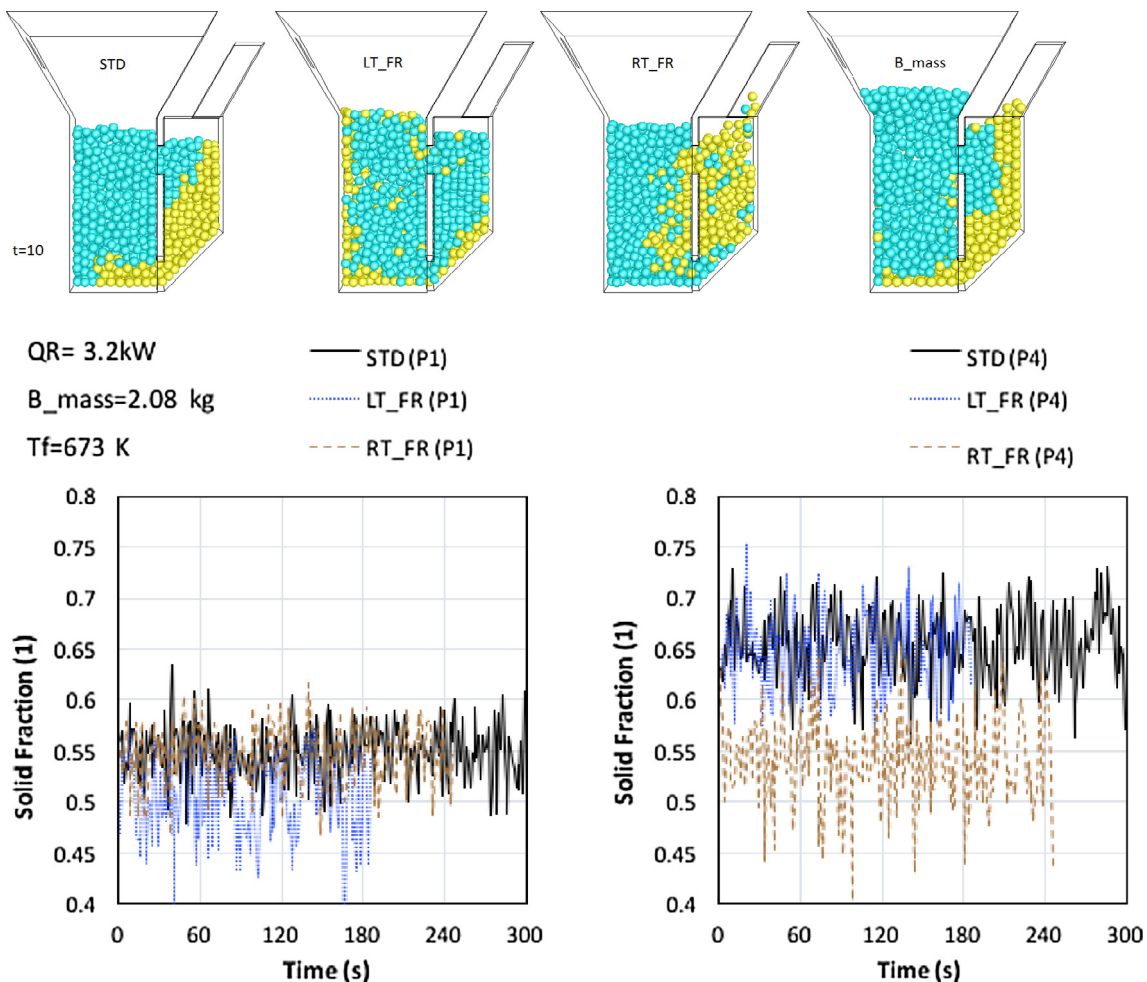
**Fig. 8.** Mean particle temperature and velocity of the left and right towers.

B) were filled in left (white) and right (blue) towers. The size of the particle typically ranges from 0.7 to 1.4 mm diameter (in which, 80% of the particles were 0.7 mm and the rest was between 0.8 and 1.4 mm). The shape and properties of the particles are same in both towers; the only variation is the color. The flow rate of the LT and RT were fixed to 70 and 30 (L/min) respectively. Instantaneous flow distribution of the particles predicted by model and captured by experiments are compared in Fig. 3. As can be seen in the figure, at the early stage, the injected air through the porous plates lifts up the particles by drag force and starts fluidization in both towers. The porosity at the bottom region of the LT increases as the particles are lifted up. Simultaneously, as the right tower porous plate is inclined by 45°, the particles in the right tower move to the left tower through the bottom interaction port. Concurrently, the particles in the top region of the left tower gradually move to the right tower through the top interaction port. Thus, the circulation of particles between the two towers occurs in clockwise direction. During the initial stages of experiments, it was observed

**Table 4**

Details of operating conditions.

Geldart type	$d_p$ ( $\mu\text{m}$ )	$U$ (m/s)		Bed mass (kg)	$T_f$ (K)	Radiation power $Q_R$ (kW)	Case name	Remarks
		LT	RT					
D	450	0.26	0.06	2.083	673	3.2	STD	Standard
D	450	0.37	0.06	2.083	673	3.2	LT_FR	Influence of LT flow rate
D	450	0.26	1.2	2.083	673	3.2	RT_FR	Influence of RT flow rate
D	450	0.26	0.06	2.083	873	3.2	IN_Tf	Influence of inlet gas temperature
D	450	0.26	0.06	2.58	673	3.2	B_Mass	Effect of bed mass
B	700–1400	0.34	0.21	0.288	–	–	VAL	Model validation

**Fig. 9.** Influence of gas flow rate on particulate flow pattern and solid volume fraction at the bottom region of left and right towers for various cases.

that a few particles (negligible amount) were left the reactor through the outlet of the RT due to the lack of space at the top region of the RT. In simulations, as the reflect boundary condition was applied to the discrete phase, the particles were returned to the reactor, which can be observed at  $t = 6$  s. As the time progresses, at the bottom interaction port, only blue color particles from the RT enters into the LT and mixed with white particles. Consequently, the mixed particles (blue and white) from the LT enters into the RT through the top interaction port. However, the ratio of blue particles is lower than white particles. Subsequently, percentage of blue particles at the LT gradually increases until the mixed particles reach the bottom interaction port through the RT. As the fluidization close to the right near wall region of the RT is low, the mixing rate is low in that region. All in all, the predicted

particulate flow pattern is in decent agreement with the experimental results. Moreover, the developed model has also been applied to predict the pressure drop of the bed of another reported study and extensively validated [40].

### 3.2. Particulate flow and temperature distribution

Following the validation, simulations were carried out for high temperature reactor made up of steel and filled with Geldart D type particles. Initially, 2.08 kg of particles, with a mean particle diameter  $450 \mu\text{m}$ , were evenly filled in both towers up to the same height. Then the reactor was placed under the solar simulator to irradiate the particles. The experimentally measured radiation flux profile [39] was used to define the radiation boundary conditions.

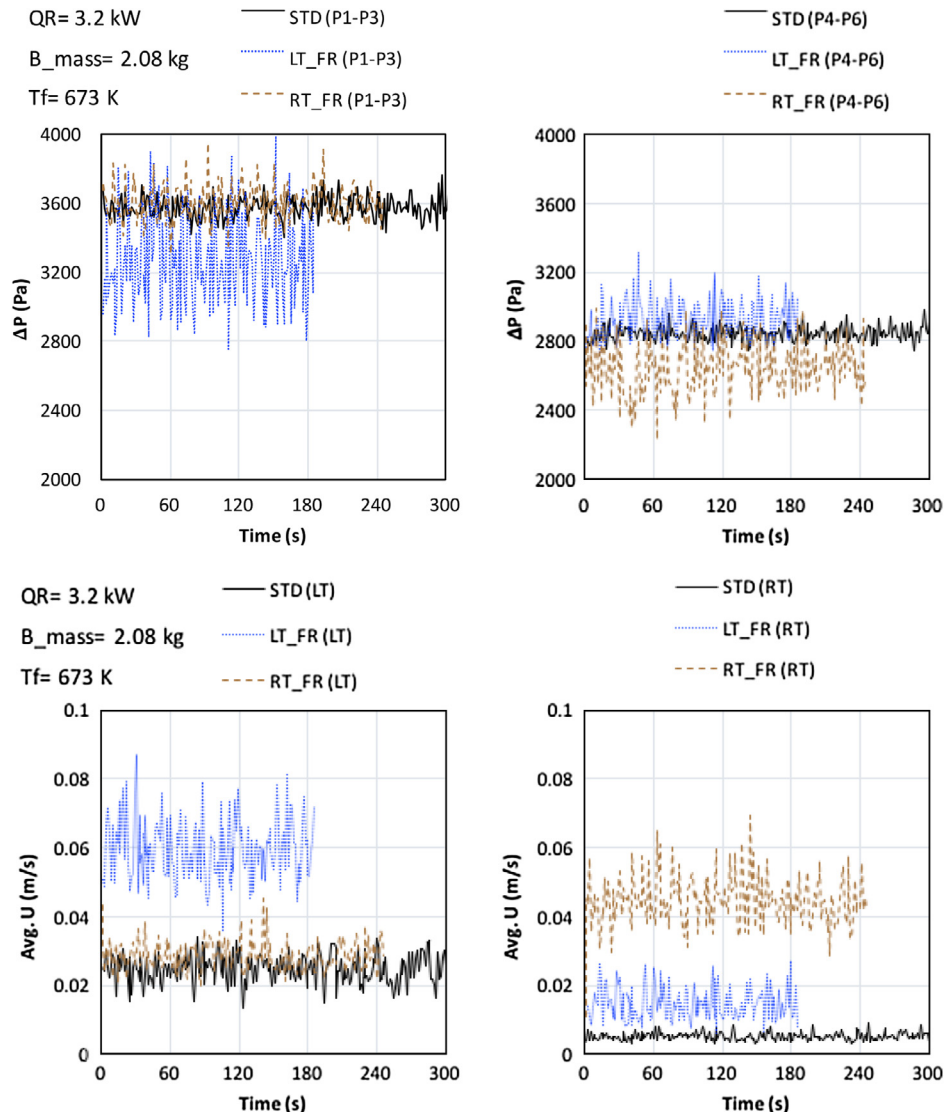


Fig. 10. Temporal variation of pressure drop and particle mean velocity of the left and right towers for various flow rates.

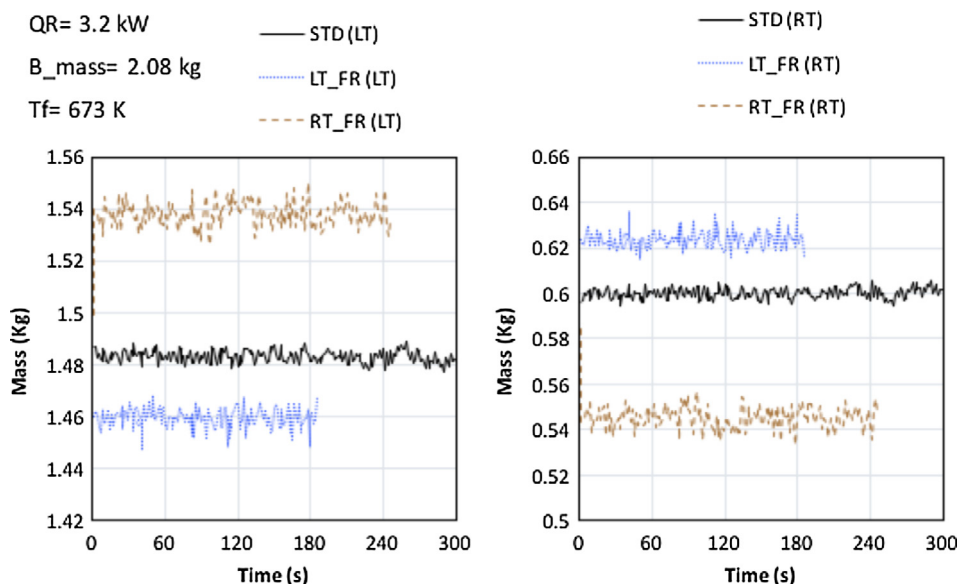
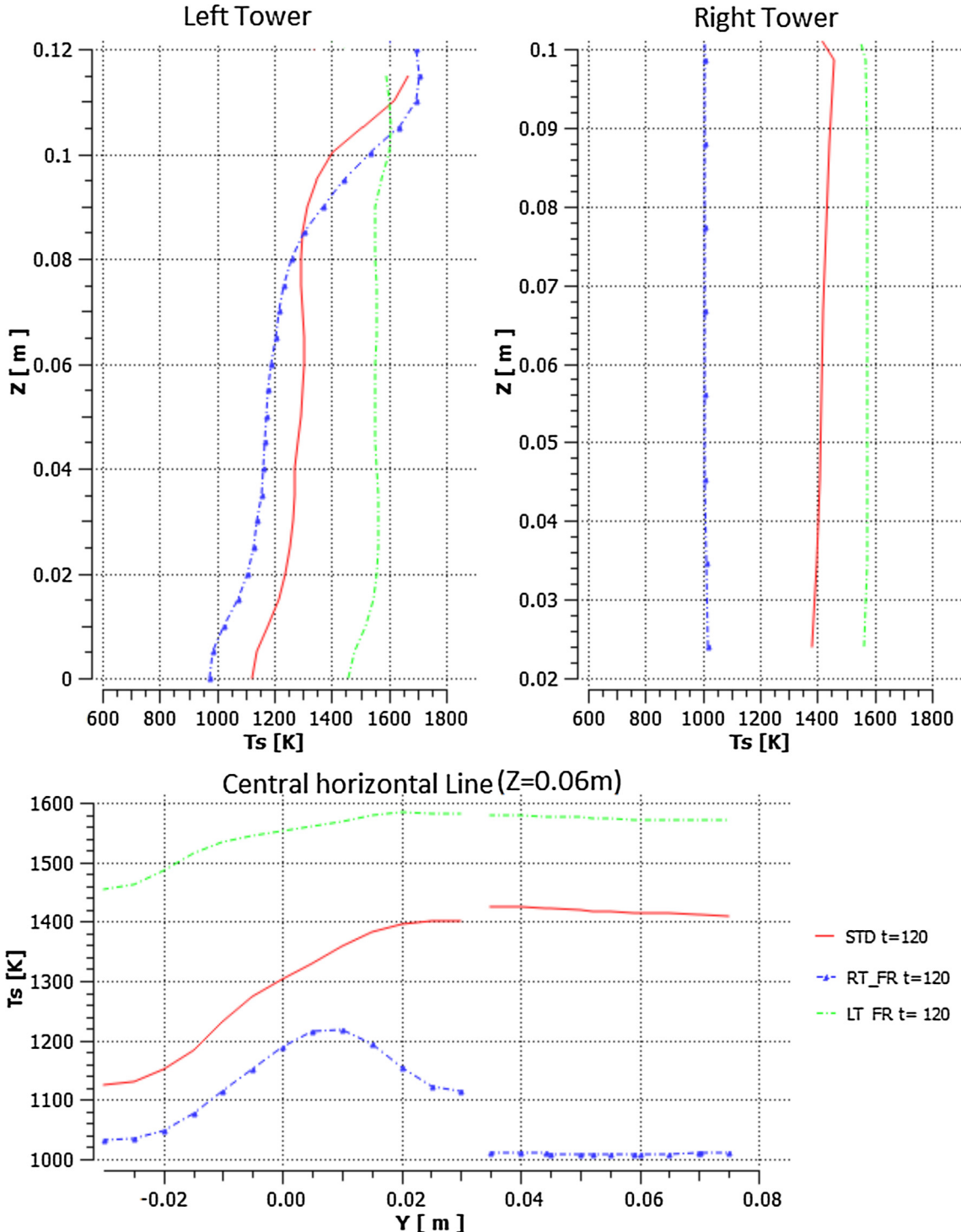


Fig. 11. Influence of gas flow rate on the total mass of the particulate phase at left and right towers as a function of time.



**Fig. 12.** Influence of gas flow rate on temperature distribution at central axial line (top) and central horizontal line (bottom) of the fluidized bed reactor at  $t = 120$  s.

The power input of the incident concentrated radiation was about  $3.2 \text{ kW}_{\text{th}}$ . The focal point was set at the height of  $0.11 \text{ m}$  of the LT. The flow rates of the left and right towers were fixed at  $4.96 \times 10^{-4}$  and  $7.20 \times 10^{-5} \text{ kg/s}$  respectively. The reactor walls were assumed as perfectly insulated. Simulation was performed for the aforementioned conditions.

Fig. 4 shows the temporal variation of particle flow pattern and solid volume fraction at different locations inside the reactor for the standard case (STD). To demonstrate the mixing of particles,

the left and right tower particles are represented by green and yellow colors. The contour figure apparently describes the flow pattern. For the given flow rate, the superficial gas velocities of the left and right towers are  $0.26 \text{ m/s}$  and  $0.06 \text{ m/s}$  respectively at  $673 \text{ K}$ . According to Wen and Yu correlation [41], the minimum fluidization velocity for the given configuration is  $0.24 \text{ m/s}$ . However, the minimum fluidization velocity decreases when the temperature of the bed increased. Initially, as the gas velocity of the left tower is higher than the minimum fluidization velocity and right

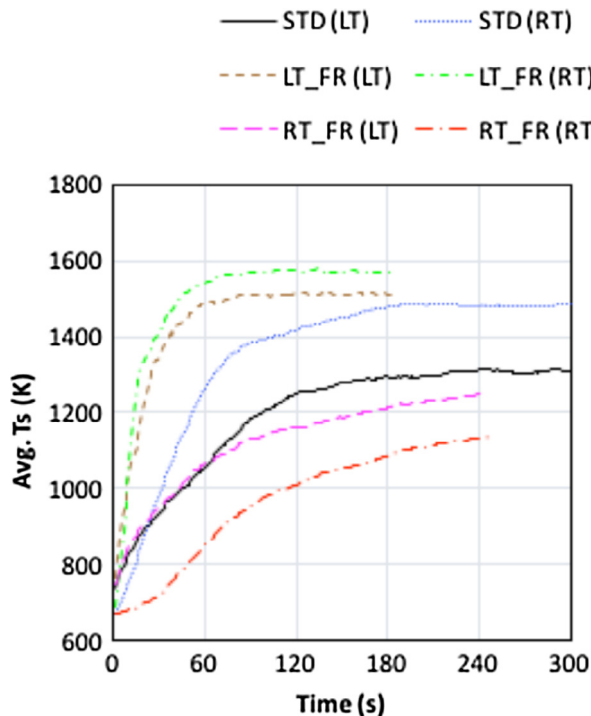


Fig. 13. Average temperature of the left and right beds for various gas flow rates as a function of time.

tower, particles of the left tower lifted up by the drag force and enter into the right tower through top interaction port, as can be seen in Fig. 4. Concurrently, the particles at the right tower move to the left tower through the bottom interaction port. Although the gas velocity of the right tower is lower than the minimum fluidization velocity, the particles in the right tower moved to left

tower. This is due to the combined effect of 45° inclined porous plate at inlet; solid fraction at bottom part of the LT is lower than the RT since the LT is fluidized; and the drag force by the inlet gas of right tower. Subsequently, the left tower particles gradually move to the right tower, in clockwise direction, and reach the bottom interaction port in 30 s. The average bed height of the left tower is higher than the right tower due to the gas velocity. Consequently, the solid volume fraction of the LT is lower than the RT. As the density of the particle is high, the solid fraction at the bottom part of the bed (P1 and P4) is higher than the top part (P3 and P6).

Fig. 5 shows the temperature at different locations and pressure drop of the left and right towers as a function of time. Initially, the bed was heated using preheaters up to 673 K. Since the top region (P3) of the left tower bed receives the direct concentrated radiation, which quickly reaches the high temperature and transfers the heat to the particles at the middle (P2) and bottom (P1) regions of the bed by convection and diffused radiation. It is noticed that the temperature of the middle region reached almost steady state later than the bottom region due to clockwise particulate flow. Due to gas velocity and bubbling fluidization, the fluctuation of the temperature profiles of the left tower is significantly higher than the right tower. The pressure drop of the right tower is lower than the left tower, approximately about 800 Pa. This could be due to the low gas velocity of the right tower.

Figs. 6 and 7 apparently describe the instantaneous temperature evolution of the left and right towers. As can be noticed in these figures, temperature of the reactor is not significantly changed after 180 s for the given conditions. Fig. 8 shows the mean particle temperature and velocity of the reactor. Using this model, a series of simulations were performed for various cases as given in Table 4 to study the influence of gas flow rate, gas temperature and total mass of the bed on temperature distribution and flow characteristics of the reactor.

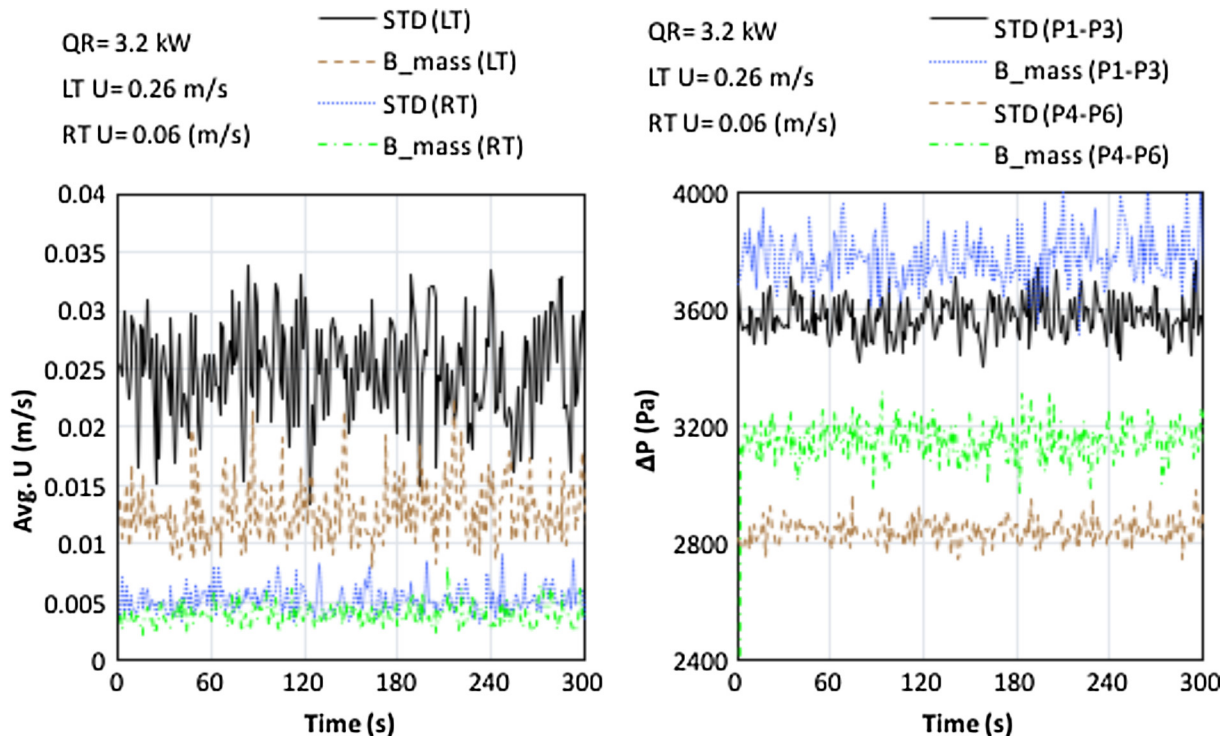
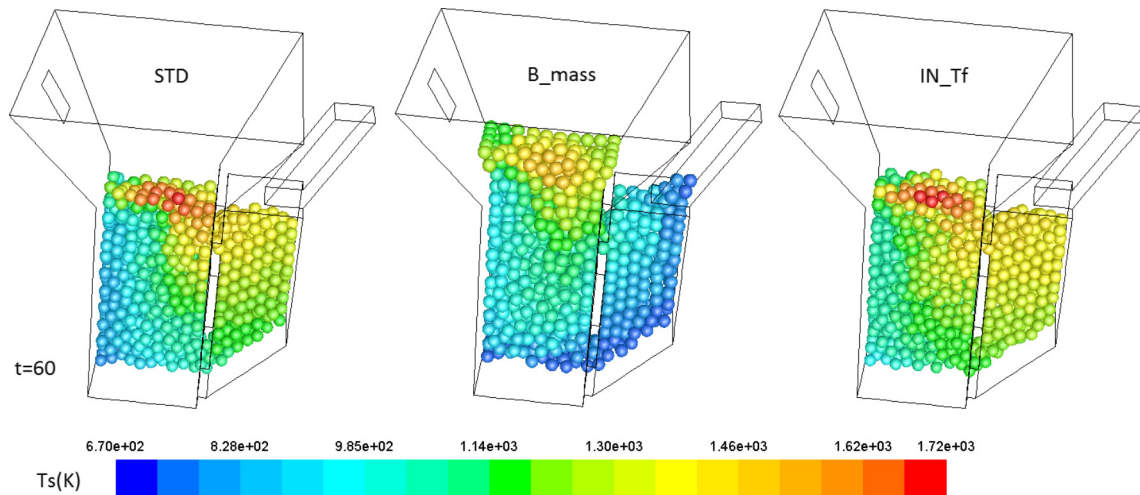
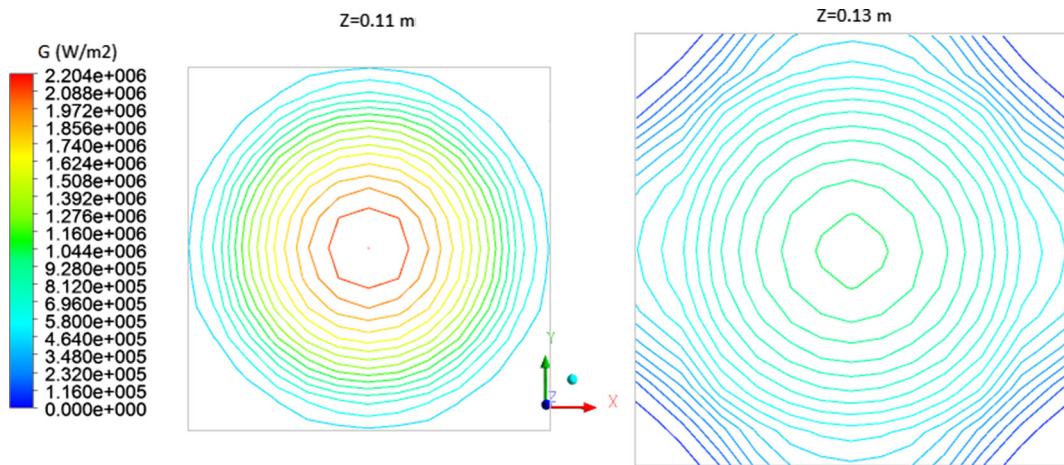


Fig. 14. Influence of bed mass on mean particle velocity and pressure drop of the bed as a function of time.



**Fig. 15.** Influence of bed mass and gas temperature on the temperature distribution of the bed at  $t = 60$  s.



**Fig. 16.** Incident radiation flux at  $Z = 0.11$  m and  $Z = 0.13$  m of the left tower.

### 3.3. Influence of gas flow rate

To investigate the effect of gas flow rate of left tower (case LT\_FR) and right tower (case RT\_FR) on temperature and particulate flow of the reactor, simulations were performed for different flow rates by keeping the other operating parameters constant. Fig. 9 shows the influence of gas flow rate on particulate flow pattern and solid volume fraction at the bottom region of the left and right towers for various cases. As can be seen in the particulate flow figure, at  $t = 10$  s, a portion of LT particles (green color) moved to RT for standard case (STD) whereas the green color particles almost completely occupied the RT when increasing the LT gas velocity. When increasing the RT gas flow rate, a portion of the RT particles (yellow color) moved to the right part of the LT as shown in the figure. Solid volume fraction at the bottom region of the bed decreases when increasing the gas flow rate as the average bed height increases. When increasing the LT gas flow rate, the solid fraction of the RT is not significantly influenced and vice versa. Fig. 10 shows the particle mean velocity and pressure drop of the left and right towers as a function of time for various flow rates. As anticipated, the pressure drop and mean velocity of the particles are decreasing and increasing respectively when increasing the gas flow rate.

Fig. 11 shows the effect of gas velocity on the total mass of the particulate phase at left and right towers as a function of time. Initially, the total mass of the discrete phase at LT and RT were 1.5165 and 0.566 kg respectively. As can be noticed in the figure, when increasing the LT flow rate, the total mass of the LT and RT are decreasing and increasing respectively. similarly, when decreasing the right tower flow rate, the total mass of the RT and LT are increasing and decreasing respectively. Fig. 12 shows the temperature distribution at central axial line (top) and central horizontal line (bottom) of the fluidized bed reactor at  $t = 120$  s for various flow rates. Residence time of the particles in the top region of LT plays a vital role on temperature distribution of the reactor. As seen in Figs. 4 and 6, the heated particles in the top region of the LT move towards the middle region and then to the RT through the top interaction port. The inlet gas flows through the bed in upward direction and extracts the heat from the heated particles by convection and leaves the tower through the outlet ports. When decreasing the velocity of the LT, the residence time of the particles increases, as a result, the irradiation duration of the top layer particles increases. Concurrently, the inlet gas cools down the particles at the bottom and middle region. Consequently, the temperature difference between the top and bottom region increases. These results are analogous to the experimental results

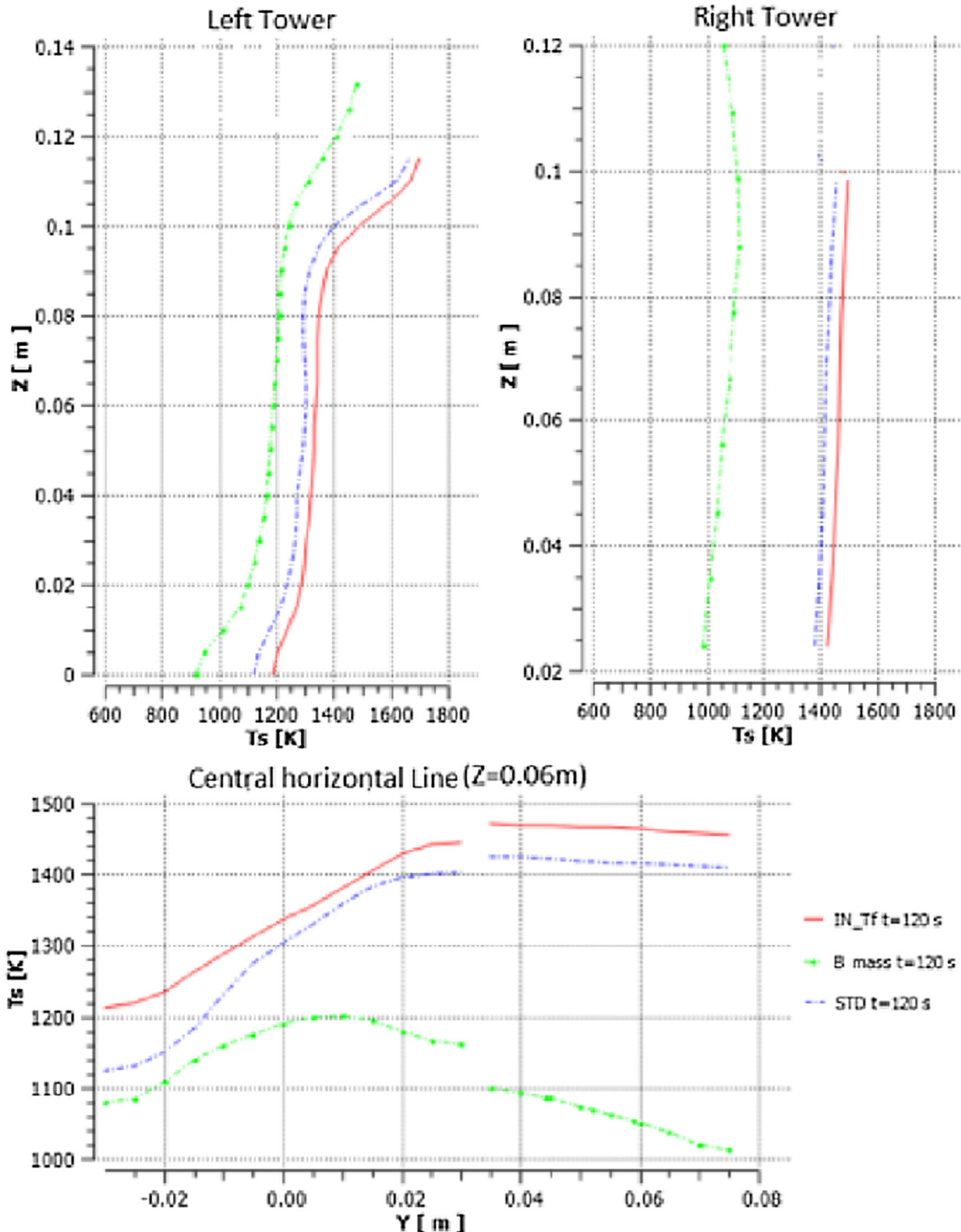


**Fig. 17.** Influence bed mass and gas temperature on temperature distribution at central axial line (top) and central horizontal line (bottom) of the fluidized bed reactor at  $t = 120\text{ s}$ .

of fluidized bed reactors [42]. When increasing the gas flow rate of LT, the bed height increases and the residence time of the particles at top region decreases, consequently, the particles transfer the heat energy to the middle and bottom region of the bed rapidly and increases the average temperature of the bed, as shown in Fig. 13. The central horizontal line profiles clearly indicate that the temperature of the particles close to the right wall of the LT is higher than the left wall as the particle flow occurs in clockwise direction.

When increasing the RT gas velocity, the particulate flow pattern apparently indicates (Fig. 9) that the RT particles move to middle region of the LT through top interaction port and gradually reaches the bottom interaction port. Consequently, the high temperature particles at the top region of the LT do not move into the RT as the clockwise particulate flow. Furthermore, the temperature of the RT decreases due to the convection of gas flow. Thus, the temperature difference between the top and bottom region of the LT increases. The centerline temperature profile changed

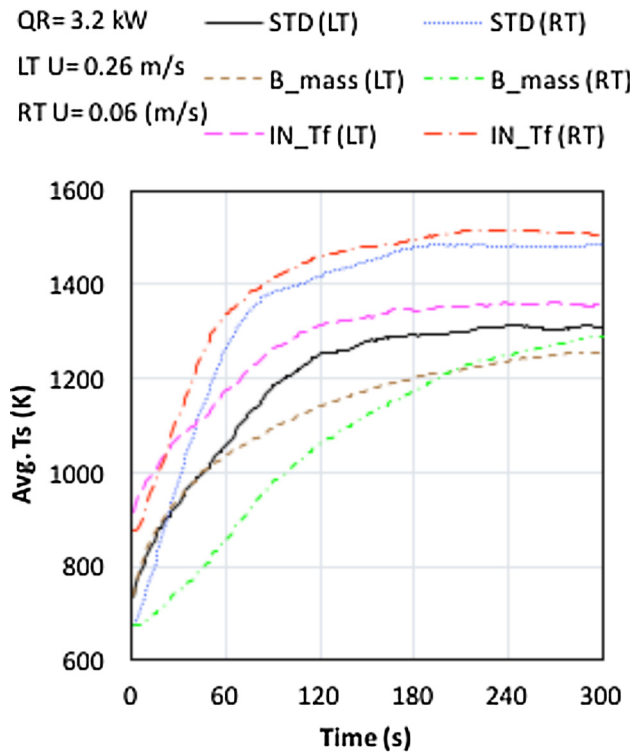


**Fig. 18.** Influence of bed mass and gas temperature on average temperature of the bed.

**Table 5**  
Peak temperature of the reactor for different cases.

Case	Peak temperature (K)
STD	1712
IN_Tf	1727
B_Mass	1503
LT_FR	1668
RT_FR	1720

into parabolic type distribution when increasing the RT flow rate and the high temperature occurs close to the central axis region. Fig. 13 show the average temperature of the left and right beds for various gas flow rates as a function of time.

#### 3.4. Influence of bed mass and gas temperature

As the thermo-fluid flow characteristics of the reactor depends on the other key operating parameters, bed mass ( $B_{\text{mass}}$ ) and inlet gas temperature ( $IN_{\text{Tf}}$ ), simulations were performed for another two cases, as given in Table 4. Fig. 14 shows the influence of bed mass on mean particle velocity and pressure drop of the bed as a function of time. As anticipated, the particle mean velocity decreases with increase in bed mass. As can be noticed in the figure, the effect of bed mass on LT particle mean velocity is higher than the RT due to the inlet gas velocity. The pressure drop of the bed increases with increase in bed mass.

Fig. 15 shows the influence of bed mass and gas inlet temperature on the temperature distribution of the bed at  $t = 60$  s. When increasing the bed mass, the average height of the bed increases, as a result, the top layer of the bed receives the diffused radiation since the focal point of the concentrated radiation slightly below the top layer. Consequently, the maximum temperature of the reactor decreases. Fig. 16 shows the incident radiation at focal

point  $z = 0.11$  m and at  $z = 0.13$  m to illustrate the maximum temperature difference between the two cases (STD and  $B_{\text{mass}}$ ). Fig. 17 show the temperature distribution at central axial line and central horizontal line of the fluidized bed reactor at  $t = 120$  s. When increasing the inlet gas temperature, the shape of the temperature profile is not significantly changed since the particulate flow pattern is same due to same flow rate and bed mass. Instead, the average temperature of the bed increases as shown in Fig. 18.

## 4. Conclusion

The heat transfer and fluidization behaviors of the two-tower fluidized bed reactor has been investigated through the CFD-DEM numerical model. An experimental visualization of particles circulation pattern and mixing of two-tower fluidized bed system has been presented. The model has been validated using the experimental results and the reported model results. Simulations have been carried out with varying gas superficial velocities, total bed masses and inlet gas temperatures. The main results obtained from this study are summarized below;

- The temperature gradient of the left tower increases when decrease in the LT flow rate and or increase in the RT flow rate.
- The influence of LT inlet velocity on the RT particle flow characteristics (porosity and velocity), and vice versa, is not significant. The average height of the LT bed increased by 12% when increasing the LT gas velocity about 30%.
- When increasing the inlet gas temperature, the average bed temperature increases whereas the flow characteristics are not significantly changed.
- The peak temperature, average temperature and velocity of the bed are decreasing with increasing the total bed mass. The effect of bed mass on LT particle mean velocity is higher than the RT and the pressure drop of the bed decreases with decrease in bed mass.
- The maximum temperature of the reactor depends on the average height of the bed and the top layer position, how far from the focal point to receive the peak radiation flux. The peak temperature of the simulated cases is summarized in Table 5.
- The developed numerical model, consists of Ergun and Wen-Yu drag model, linear-spring dashpot model and discrete ordinate radiation model, can be used to improve the design of the two-tower type fluidized bed receivers for beam-down concentrating system.

## Acknowledgement

This study has been supported by the Tenure Track Program, The Ministry of Education, Culture and Sports, Science and Technology of Japan.

## Conflict of interest

The author declared that there is no conflict of interest.

## References

- H.M. Abdelmalib, M.A.M. Youssef, A.A. Hassan, S.B. Youn, I. Tae Im, Heat transfer process in gas-solid fluidized bed combustors: a review, *Int. J. Heat Mass Transf.* 89 (2015) 567–575.
- Q. Wang, Y. Feng, J. Lu, W. Yin, H. Yang, P.J. Witt, M. Zhang, Numerical study of particle segregation in a coal beneficiation fluidized bed by a TFM-DEM hybrid

- model: influence of coal particle size and density, *Chem. Eng. J.* 260 (2015) 240–257.
- [3] A.V. Patil, E.A.J.F. Peters, V.S. Sutkar, N.G. Deen, J.A.M. Kuipers, A study of heat transfer in fluidized beds using an integrated DIA/PIV/IR technique, *Chem. Eng. J.* 259 (2015) 90–106.
- [4] L. Lu, A. Morris, T. Li, S. Benyahia, Extension of a coarse-grained particle method to simulate heat transfer in fluidized beds, *Int. J. Heat Mass Transf.* 111 (2017) 723–735.
- [5] J.R. Van Ommen, R.F. Mudde, Measuring the gas–solids distribution in fluidized beds – a review, *Int. J. Chem. React. Eng.* 6 (2008) 1542–6580.
- [6] Y. Tsuji, T. Kawaguchi, T. Tanaka, Discrete particle simulation of two-dimensional fluidized bed, *Powder Technol.* 77 (1993) 79–87.
- [7] G. Zhang, M. Gutierrez, M. Li, A coupled CFD-DEM approach to model particle–fluid mixture transport between two parallel plates to improve understanding of proppant micromechanics in hydraulic fractures, *Powder Technol.* 308 (2017) 235–248.
- [8] H. Zhang, A. Yu, W. Zhong, Y. Tan, A combined TLBM–IBM–DEM scheme for simulating isothermal particulate flow in fluid, *Int. J. Heat Mass Transf.* 91 (2015) 178–189.
- [9] Q.F. Hou, Z.Y. Zhou, A.B. Yu, Computational study of heat transfer in a bubbling fluidized bed with a horizontal tube, *AIChE J.* 58 (2012) 1422–1434.
- [10] Y. Zhao, M. Jiang, Y. Liu, J. Zheng, Particle-scale simulation of the flow and heat transfer behaviors in fluidized bed with immersed tube, *AIChE J.* 55 (2009) 3109–3124.
- [11] H. Wahyudi, K. Chu, A. Yu, 3D particle-scale modeling of gas–solids flow and heat transfer in fluidized beds with an immersed tube, *Int. J. Heat Mass Transf.* 97 (2016) 521–537.
- [12] N. Gui, J.R. Fan, S. Chen, Numerical study of particle–particle collision in swirling jets: a DEM–DNS coupling simulation, *Chem. Eng. Sci.* 65 (2010) 3268–3278.
- [13] W. Zhong, Y. Xiong, Z. Yuan, M. Zhang, DEM simulation of gas–solid flow behaviors in spout–fluid bed, *Chem. Eng. Sci.* 61 (2006) 1571–1584.
- [14] S. Benyahia, J.E. Galvin, Estimation of numerical errors related to some basic assumptions in discrete particle methods, *Ind. Eng. Chem. Res.* 49 (2010) 10588–10605.
- [15] M.A. Mokhtar, K. Kuwagi, T. Takami, H. Hirano, M. Horio, Validation of the similar particle assembly (SPA) model for the fluidization of Geldart's group A and D particles, *AIChE J.* 58 (2012) 87–98.
- [16] H.R. Norouzi, R. Zarghami, N. Mostoufi, New hybrid CPU-GPU solver for CFD-DEM simulation of fluidized beds, *Powder Technol.* 10.1016/j.powtec.2016.11.061.
- [17] K.W. Chu, B. Wang, D.L. Xu, Y.X. Chen, A.B. Yu, CFD–DEM simulation of the gas–solid flow in a cyclone separator, *Chem. Eng. Sci.* 66 (2011) 834–847.
- [18] S.B. Kuang, A.B. Yu, Micromechanic modeling and analysis of the flow regimes in horizontal pneumatic conveying, *AIChE J.* 57 (2011) 2708–2725.
- [19] T. Kodama, N. Gokon, Thermochemical cycles for high-temperature solar hydrogen production, *Chem. Rev.* 107 (2007) 4048–4077.
- [20] World Energy Outlook, IEA (International Energy Agency), 2014. <<http://www.worldenergyoutlook.org>>.
- [21] G. Flamant, D. Gauthier, C. Boudhari, Y. Flitris, A 50 kW fluidized bed high temperature solar receiver: heat transfer analysis, *J. Sol. Energy Eng.* 110 (1988) 313–320.
- [22] B. Sakadjian, S. Hu, M. Maryamchik, T. Flynn, K. Santelmann, Z. Ma, Fluidized-bed technology enabling the integration of high temperature solar receiver CSP systems with steam and advanced power cycles, *Energy Proc.* 69 (2015) 1404–1411.
- [23] P. Salatino, P. Ammendola, P. Bareschino, R. Chirone, R. Solimene, Improving the thermal performance of fluidized beds for concentrated solar power and thermal energy storage, *Powder Technol.* 290 (2016) 97–101.
- [24] C. Tregambi, R. Chirone, F. Montagnaro, P. Salatino, R. Solimene, Heat transfer in directly irradiated fluidized beds, *Sol. Energy* 129 (2016) 85–100.
- [25] S. Migliozi, A. Paulillo, R. Chirone, P. Salatino, R. Solimene, Hydrodynamics of compartmented fluidized beds under uneven fluidization conditions, *Powder Technol.* 316 (2017) 476–491.
- [26] P. Ammendola, P. Bareschino, R. Chirone, P. Salatino, R. Solimene, Controlling thermal properties of dense gas fluidized beds for concentrated solar power by internal and external solids circulation 2017, in: AIP Conference Proceedings (SolarPACES 2016) 1850 Art. No. 80003.
- [27] A. Steinfeld, Solar thermochemical production of hydrogen—a review, *Sol. Energy* 78 (2005) 603–615.
- [28] N. Gokon, T. Mataga, N. Kondo, T. Kodama, Thermochemical two-step water splitting by internally circulating fluidized bed of NiFe<sub>2</sub>O<sub>4</sub> particles: successive reaction of thermal-reduction and water-decomposition steps, *Int. J. Hydrogen Energy* 36 (2011) 4757–4767.
- [29] T. Kodama, N. Gokon, S. Enomoto, S. Itoh, T. Hatamachi, Coal coke gasification in a windowed solar chemical reactor for beam-down optics, *J. Sol. Energy Eng.* 132 (2010) 1–6, 041004.
- [30] T. Kodama, S. Bellan, N. Gokon, H.S. Cho, Particle reactors for solar thermochemical processes, *Sol. Energy* 10.1016/j.solener.2017.05.084.
- [31] K. Matsubara, Y. Kazuma, A. Sakurai, S. Suzuki, L. Soon-Jae, T. Kodama, N. Gokon, High-temperature fluidized receiver for concentrated solar radiation by a beam-down reflector system, *Energy Proc.* 49 (2014) 447–456.
- [32] K. Matsubara, H. Sakai, Y. Kazuma, A. Sakurai, T. Kodama, N. Gokon, H.S. Cho, K. Yoshida, Numerical modeling of a two-tower type fluidized receiver for high temperature solar concentration by a beam-down reflector system, *Energy Proc.* 69 (2015) 487–496.
- [33] S. Ergun, Fluid flow through packed columns, *Chem. Eng. Prog.* 48 (1952) 89–94.
- [34] Y.C. Wen, Y.H. Yu, Mechanics of fluidization, *Chem. Eng. Prog. Symp. Ser.* 62 (1966) 100–111.
- [35] Ansys Fluent Theory Guide, Release 17.0, Ansys Inc., Canonsburg, PA, USA, 2016.
- [36] D.J. Gunn, Transfer of heat or mass to particles in fixed and fluidised beds, *Int. J. Heat Mass Transf.* 21 (4) (1978) 467–476.
- [37] P.A. Cundall, D.L. Strack, A discrete numerical model for granular assemblies, *Geotechnique* 29 (1979) 47.
- [38] A.V. Patil, E.A.J.F. Peters, J.A.M. Kuipers, Comparison of CFD–DEM heat transfer simulations with infrared/visual measurements, *Chem. Eng. J.* 277 (2015) 388–401.
- [39] N. Gokon, T. Izawa, T. Abe, T. Kodama, Steam gasification of coal cokes in an internally circulating fluidized bed of thermal storage material for solar thermochemical processes, *Int. J. Hydrogen Energy* 39 (2014) 11082–11093.
- [40] S. Bellan, K. Matsubara, C.H. Cheok, N. Gokon, T. Kodama, CFD-DEM investigation of particles circulation pattern of two-tower fluidized bed reactor for beam-down solar concentrating system, *Powder Technol.* 319 (2017) 228–237.
- [41] C.Y. Wen, Y.H. Yu, A generalized method for predicting the minimum fluidization velocity, *AIChE J.* 12 (1966) 610–612.
- [42] N. Gokon, R. Ono, T. Hatamachi, L. Liuyun, H.J. Kim, T. Kodama, CO<sub>2</sub> gasification of coal cokes using internally circulating fluidized bed reactor by concentrated Xe-light irradiation for solar gasification, *Int. J. Hydrogen Energy* 37 (2012) 12128–12137.